Multi-function vortex array radar ⊘

Xiaofei Li ⓘ ; Sajjad Bashiri; Vasilisa Ponomarenko ⓘ ; Yu Wang ⓘ ; Yangjian Cai ✉ ⓘ ;
Sergey A. Ponomarenko ✉ ⓘ

Check for updates
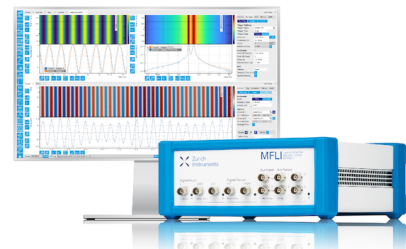
View Online

Export Citation

AIP Publishing

Multi-function vortex array radar

Xiaofei Li,[1,2] (iD) Sajjad Bashiri,[1] Vasilisa Ponomarenko,[3] (iD) Yu Wang,[4] (iD) Yangjian Cai,[2,a] (iD)
and Sergey A. Ponomarenko[1,5,a] (iD)

AFFILIATIONS

[1]Department of Electrical and Computer Engineering, Dalhousie University, Halifax, Nova Scotia B3J 2X4, Canada
[2]Shandong Provincial Engineering and Technical Center of Light Manipulation and Shandong Provincial Key Laboratory
  of Optics and Photonic Devices, School of Physics and Electronics, Shandong Normal University, Jinan 250014, China
[3]Department of Electrical Engineering and Computer Science, University of California Berkeley, Berkeley, California 94720, USA
[4]School of Information Science and Engineering, Shandong Normal University, Jinan 250014, China
[5]Department of Physics and Atmospheric Science, Dalhousie University, Halifax, Nova Scotia B3H 4R2, Canada

[a]Authors to whom correspondence should be addressed: yangjiancai@sdnu.edu.cn and serpo@dal.ca

ABSTRACT

In the realm of automation systems, multi-function radars serve as essential sensory components for self-driving vehicles and airbornes. Effective resource allocation management is crucial, requiring a high level of versatility to accomplish multiple tasks, especially, for increasingly miniaturized hardware. Here, we advance a balanced protocol for detecting, positioning, and tracking moving targets in real-time. Our protocol integrates efficient data processing methods with robust hardware. Specifically, detection signals are modulated by optical vortices for imaging, and real time processing of the image field facilitates target positioning and tracking. Moreover, the protocol extends its utility to serve as a topographic laser profiling system for natural landscapes, highlighting its adaptability. This adaptability and versatility well position the proposed protocol to support a wide range of applications, spanning self-driving vehicles and aerial systems, underscoring its potential significance across multiple platforms.

Radar systems, with their ability to detect and track objects by transmitting electromagnetic waves and analyzing their reflections, play an important role in various fields,[1,2] including weather monitoring,[3,4] autonomous navigation,[5] and remote sensing.[6] However, the emerging applications demand radar systems capable of simultaneously performing several tasks. For example, automation systems for self-driving vehicles rely heavily on abundant detected information. A reliable automation system should support real-time decisions and responses, necessitating the radar systems that can synchronize multiple missions, such as ranging, positioning, and speed estimation, within a single imaging protocol. As a response to this challenge, the concept of multi-function radar (MFR) has emerged,[7] which focuses on a primary mission while handling secondary tasks, thereby significantly enhancing the value of the obtained information.

To meet multiple requirements, the effective management of limited radar resources to accomplish multiple tasks of scheduling time, energy, and computational resources for each task presents the primary challenge in multi-function radar system design.[8] Various resource management schemes have been explored to enhance the performance of MFR for different tasks. Hardware-based schemes can provide services for both aircraft and weather surveillance,[3,9] and can also perform single target tracking and classification.[10] Furthermore, protocols involving data processing algorithms can handle multiple target tracking,[11] people counting and motion recognition,[12] as well as the detection and tracking of pedestrians and vehicles.[13] Although hardware-based resource management demonstrates robust performance and efficiency, integrating new hardware components with the existing systems can be complex, time-consuming, and costly.[14] However, signal processing methods optimize the use of resources and offer flexibility in various scenarios with crucial adaptability, particularly for the gradually integrating miniaturized radars.[15] Therefore, considering the balance of these aspects for innovative management, a compromise scheme that incorporates the benefits of both hardware-based and signal processing methods is required.

During this decade, advancements in radar technology have been primarily driven by a compromise technology, the signal modulation for subsequent detection. One remarkable development is the incorporation of orbital angular momentum (OAM) of light into radar systems, where OAM arises due to a helical wavefront $\exp(il\theta)$ of the optical field.[16] By using electromagnetic wave modulated by OAM, the

radar system can significantly improve image resolution and collect more information about the target,[17,18] even in low signal-to-noise ratio (SNR) environments.[19] Additionally, research reports indicate that OAM carries great promise for estimating target velocities[20] and enabling three-dimensional (3D) imaging.[21] Simultaneously, investigations into data processing algorithms for vortex radar are ongoing.[22] These advancements exemplify transformative potential of OAM in MFR systems.

In this work, we introduce a task management protocol for MFR by combining phase-array vortex modulation and laser radar technologies. We employ an optical vortex array for signal detection and an appropriate data processing approach to synchronize imaging, positioning, and velocity estimation. Our study presents a comprehensive imaging scheme for two-dimensional (2D) targets, demonstrating how Poynting vector flow and power calculations of the total image field facilitate the determination of azimuth and radial position of the target. Furthermore, we extend the proposed protocol to include topographic applications by developing an imaging scenario for 3D targets. These findings illustrate the capacity of our protocol for hardware-based management and data processing that widen the scope of MFR system applications.

We sketch the vortex MFR geometry and schematic diagram of our protocol in Fig. 1. The source field $E_0(\mathbf{r}')$ of the radar is emitted into free space and reaches the target plane after free-space propagation. The electrical field $E(\mathbf{r})$ arriving at the target plane can be expressed, in the paraxial approximation, by the Fresnel integral

(a)

Reflected field

Emitted field

(b)

Source $E_0(\mathbf{r}')$ (r', θ')

Target $E(\mathbf{r})$ (r, θ)

Receiver $E_r(\boldsymbol{\rho})$

Image $E_{im}(\boldsymbol{\rho}')$

FIG. 1. Concept (a) and protocol schematics (b) of vortex MFR.

$$E(\mathbf{r}) \propto \int d\mathbf{r}' \, E_0(\mathbf{r}') \exp\left[\frac{ik(\mathbf{r} - \mathbf{r}')^2}{2z}\right]. \qquad (1)$$

The source field in our protocol is generated by a vortex beam array. We produce the array from an input Gaussian laser beam illuminating a phased-modulation element, such as a spatial light modulator (SLM), say, loaded with a customized set of holograms. We assume that the coordinates of a point $\mathbf{r}'$ in the SLM plane are represented by (x', y'). To generate the source field $E_0(x', y')$, we endow the field of the input Gaussian beam with the phase

$$\sum_{n=1}^{N} \exp\left[-\frac{ik}{f}(x_n x' + y_n y')\right] \exp(il\theta'). \qquad (2)$$

Here, N is the total number of identical optical vortices (OV) with the topological charge l composing the array. All vortices are located at the vertices of a regular N-sided polygon inscribed into a circle of radius r_n. The center of the circle marks the array center with Cartesian coordinates (x_c, y_c). The nth OV within the array is situated at the point with coordinates $x_n = r_n \cos\theta_n + x_c$ and $y_n = r_n \sin\theta_n + y_c$, where $\theta_n = 2\pi n/N$. We sketch the vortex array geometry in Fig. 2(a). The gauge transformation of Eq. (2) allows us to shift the overall array or individual vortices within the array via phase modulation realized with the aid of a thin lens of focal length f.

The monostatic radar operates as follows. First the source field, having reached the target, is reflected back to the source/receiver along a straight-line path. The reflected field $E_r(\boldsymbol{\rho})$ registered by the receiver then reads

$$E_r(\boldsymbol{\rho}) \propto \int d\mathbf{r} \, E(\mathbf{r}) O(\mathbf{r}) \exp\left[\frac{ik(\boldsymbol{\rho} - \mathbf{r})^2}{2z}\right], \qquad (3)$$

where $O(\mathbf{r})$ is an aperture function of the target. Second, we obtain the image field $E_{im}(\boldsymbol{\rho}')$ via a Fourier transformation of the received one using the lens of focal length f as[23]

$$E_{im}(\boldsymbol{\rho}') \propto \int d\boldsymbol{\rho} \, E_r(\boldsymbol{\rho}) \exp\left(\frac{-ik\boldsymbol{\rho} \cdot \boldsymbol{\rho}'}{f}\right). \qquad (4)$$

To showcase the performance of our protocol, we present several recovered images of variable texture, complexity, and grayscale range, including the logo of Dalhousie and two standard test images: Happyfish and Cameraman. We model these grayscale images (from 0 to 255) as 2D targets $O(\mathbf{r})$ with normalized gray levels used as reflection coefficient indicators. Hereafter, we consider vortex arrays comprised of nine OVs with $l = 2$, placed on the ring of radius $r_n = 4.5$ mm. Furthermore, we first assume an ideal scenario whereby the radar precisely locks onto the target, so that the center of the vortex array is perfectly aligned with the target center. The target is located 1500 m away from the source. By utilizing Eqs. (1)–(4), we display the target images in Fig. 2(b). Good resemblance between the objects and images points to excellent accuracy of our MFR protocol in this idealized situation.

In general, however, the array and target centers are misaligned, resulting in poor image quality and scarce resemblance of the image to the target, especially for moving targets. Hence, precise target position acquisition, which must incorporate accurate orientation information, is crucial to achieve optimal imaging results. The MFR is expected to
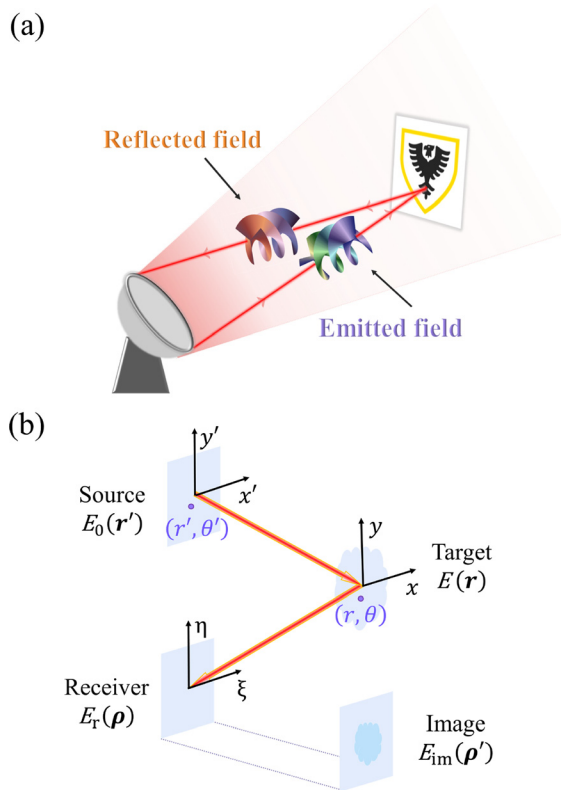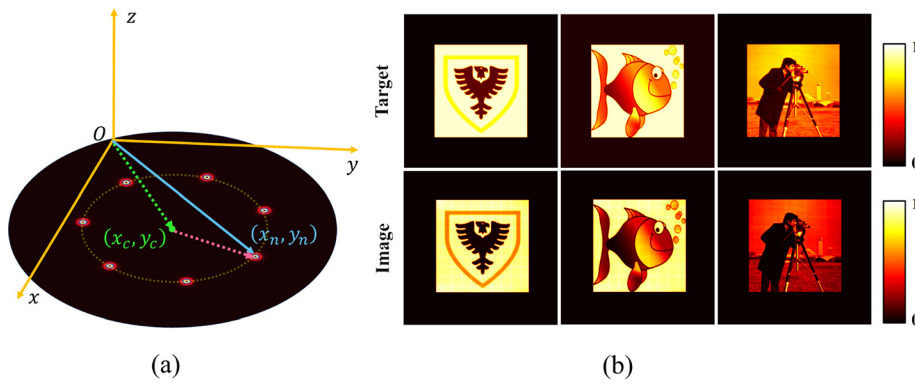
FIG. 2. Geometry of the vortex array (a) and recovered images (b).

extract additional implicit information from the image plane, which can effectively guide the system to accurately track a moving target, at least, as far as providing azimuth or radial references for the subsequent detection procedure is concerned. To realize this idea within our MFR, we carried out further simulations.

The target position acquisition procedure involves extracting information about a relative position of the array and target centers. To this end, we start by setting up our polar coordinate system in the target plane, with the array center serving as the origin. The target center, marked by a red solid point, is located at a point with the radius vector $r = (r, \theta)$ [see Fig. 3(a)]. Adjusting (r, θ), we can control the relative position of the two centers, thereby enabling target movement tracking. The target acquisition process entails detecting the azimuthal angles [Fig. 3(b)] and radial distances [Fig. 3(c)] of the relative position vector. Our primary goal is to determine θ of the target center relative to x-axis. As depicted in Fig. 3(b), we evaluate misalignment for seven different angles separated by the same interval of $\pi/4$ at a fixed relative radius of $r = 16$ m. Repeating the tracking protocol yields the results shown in Figs. 4(b)–4(h). For better comparison, we also display the "perfect" case with the aligned array and target centers in Fig. 4(a). As anticipated, due to the source–target misalignment, we can observe image distortions, which are related to azimuthal misalignment. These results further highlight the importance of optimal array positioning to attain optimal image quality. To obtain the azimuth direction of the relative position of the target relative to the array center, we evaluate the Poynting vector of the imaged electromagnetic field.[16] The former yields us the direction of electromagnetic energy flow and is defined as

$\vec{S}_\perp = \frac{i}{4\eta_0 k}(E_{im}\vec{\nabla}_\perp E_{im}^* - E_{im}^*\vec{\nabla}_\perp E_{im})$. We exhibit the transverse power flow distributions for each case in Figs. 4(b)–4(h) by the arrows. We can infer from the figure that the power flow direction is affected by the relative azimuth, indicating that the flow distribution determines the azimuth direction, which facilitates target tracking. For instance, when the target center is located at $(16\,m, \pi/4)$, the energy flow direction aligns with the angle the target center makes with x-axis [see Fig. 4(c)]. In the perfect alignment situation, however, a perfect image can be acquired, which is characterized by a nearly isotropic energy flow [see Fig. 4(a)].

In addition, we aim to determine the radial distance r between the target and array centers. As is illustrated in Fig. 3(c), we consider six cases featuring three different radii ($r = 9.5, 12.7, 16.2$ m) across two azimuthal directions, 0 and $2\pi/3$. We display the corresponding images and the corresponding transverse power flow distributions (indicated by arrows) in Fig. 5. Figures 5(a)–5(f) support the earlier conclusions regarding the role of the source–target azimuth for correct target acquisition. However, the flow distribution in the case of partially recovered images only specifies the azimuth direction and does not provide any valid information about the radial position of the target. Therefore, to determine the distance to the target, we work out the total power carried by the image field as $P = \int d\boldsymbol{\rho}' E_{im}(\boldsymbol{\rho}')$. To study the dependence of the total power P on relative distance r further, we examine the total power as a function of the radial distance between the centers for two azimuth directions, 0 and $2\pi/3$, and display it in panels (g) and (h) of Fig. 5. It follows that as the source–target distance gradually increases, so does the total power, although the power
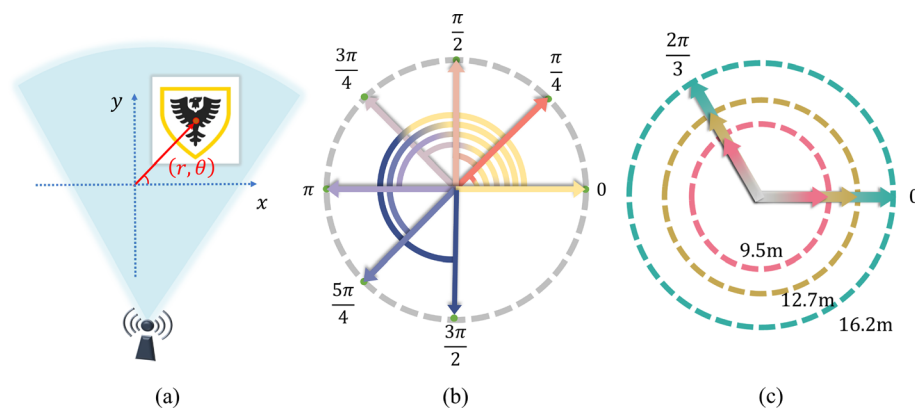

FIG. 3. Target acquisition of the proposed vortex MFR (a) with variable azimuth (b) and relative radial position of the array and target centers (c).
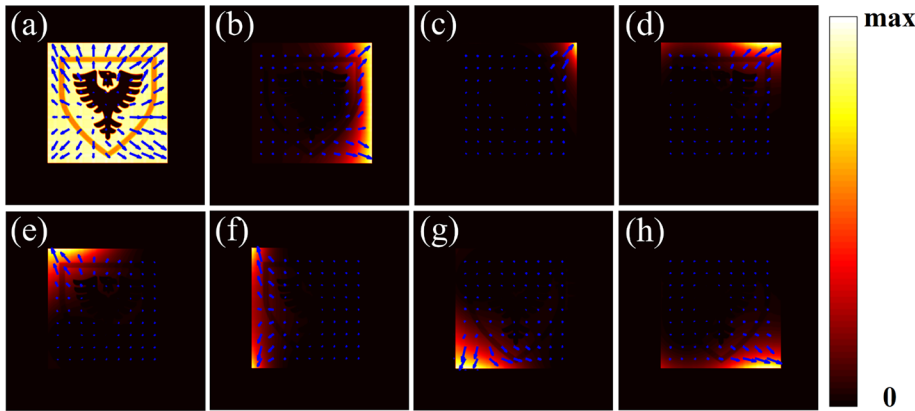
FIG. 4. Recovered image and the corresponding transverse power flow distributions for a variable azimuth.

growth is non-uniform across different radii. Moreover, a comparison of the two panels indicates that the power growth is affected by the azimuth. In the short distance range (0–15 m), the power flow slightly increases with the distance and only marginally depends on the azimuth. As the radial distance between the centers reaches the range 15–20 m, the power growth rate difference in the two directions becomes noticeable. This observation highlights a nuanced interplay between the azimuth direction and the power evolution as a function of the radial separation distance. Ultimately, this dependence ascertains the magnitude of the radial separation between the target and array centers, allowing the radar system to accurately locate the target during each scan.

FIG. 5. Recovered images and the corresponding transverse power flow distributions for a variable array-target separation distance 9.5, 12.7, 16.2 m in directions corresponding to the angles 0 (a)–(c) and $2\pi/3$ (d)–(f). Power curves vs the separation distance r for azimuthal directions 0 (g) and $2\pi/3$ (h), respectively.

To summarize, we can complete the target acquisition process in two consecutive steps. First, we determine the azimuth of the target by evaluating the Poynting vector flow. Second, we elucidate the corresponding radial distance from the array to the target center by analyzing the total power associated with said azimuth. Consequently, we can extract the crucial target orientation information through the analysis of the power distribution of the received field. Moreover, we can also estimate the velocity of a moving target. By comparing the power curves of two consecutive scans, we can infer the distance the target has traveled between the scans, thereby estimating its velocity. Subsequently, integrating the target's position with its velocity allows us to forecast its future motion path. We can then use the acquired information to adjust the array center in real time to have the radar lock onto the moving target, thereby ensuring continuous tracking.
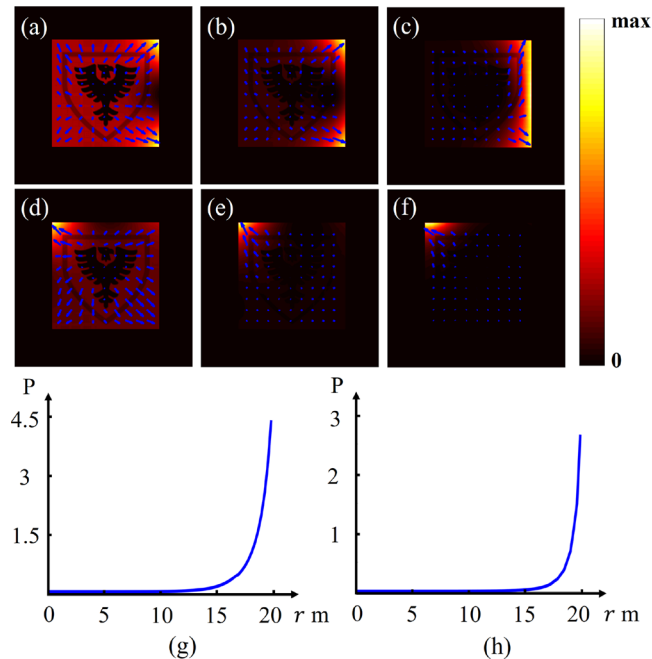
Our simulations indicate that the peak intensity of the 2D image field is moderately influenced by the distance to the target. We can then acquire a 3D image by figuring out the distance to each point on the target surface and accumulating these distance measurements to construct a point cloud representation of the target [as depicted in Fig. 6(a)]. Notably, laser radar systems have the capability to directly assess the landscape while circumnavigating geometric distortion issues.[24,25] In this connection, one might wonder whether the proposed MFR protocol is capable of 3D imaging and sensing. Hence, we explore the potential of our protocol for topographic laser profiling.

To this end, we exhibit a 3D landscape in Fig. 6(a), together with the results of its reconstruction within our protocol. We assume, for simplicity, that the reflectivity index of the mountain surface is unity, $O(x, y) = 1$. As is seen in Fig. 6(b), we denote the height at the point in the ith column and jth row of a matrix representation (x_i, y_j) of the target surface by h_{ij} and place a light source a distance d above the ground. Furthermore, we denote the detection distance from the source to each point by z_{ij}. We can then write down the electrical field $E(x_i, y_j)$ at each point on the terrain surface in terms of the Fresnel integral as

$$\mathbf{E}(x_i, y_j) \propto \int d\mathbf{r}' \mathbf{E}_0(\mathbf{r}') \exp\left\{\frac{ik\left[(x_i - x')^2 + (y_j - y')^2\right]}{2z_{ij}}\right\}. \quad (5)$$
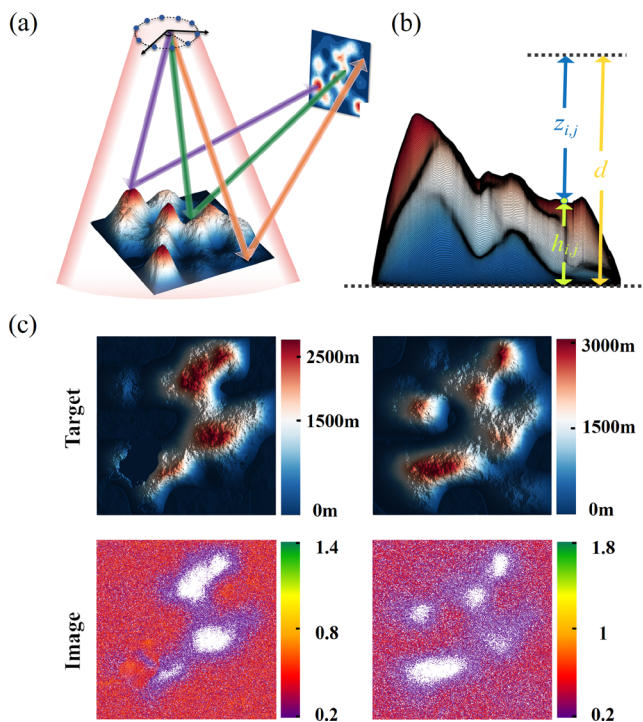
The field of the echo signal at the receiver then reads

28 October 2024 15:28:17

FIG. 6. 3D and 2D views of the schematics of the terrain profiling process.

$$\mathbf{E}_r(\xi_i, \eta_j) \propto \int d\mathbf{r} \mathbf{E}(\mathbf{r}) O(\mathbf{r}) \exp\left\{ \frac{ik\left[(\xi_i - x)^2\right]}{2z_{ij}} \right\}$$

$$\times \exp\left\{ \frac{ik\left[(\eta_j - y)^2\right]}{2z_{ij}} \right\}. \tag{6}$$

By utilizing Eqs. (5) and (6), we map the terrain features of two modeled target landscapes as displayed in Fig. 6(c). The two examples we provide have different terrain distributions and altitude maxima. In the left column, the source is located at a distance $d = 3270$ m, whereas in the right one, it is placed $d = 3570$ m away from the ground. The comparison of the target and image landscapes reveals that the generated 2D contour patterns derived from the point clouds closely match the visual depiction of the terrains in 2D view. The similarity between the reconstructed patterns and the actual landscapes highlights the efficacy of our protocol in translating point cloud data into meaningful 2D landscape representations. On comparing the two columns of Fig. 6(c), we observe that the maximum image intensity is indeed related to the altitude range of the original target. These results underscore the versatility and adaptability of our protocol, indicating its potential to address a wider range of scenarios beyond the current context.

In conclusion, we have introduced and illustrated a protocol realizing a multi-function radar employing an optical vortex array. Our protocol integrates the benefits of both hardware-based management and signal processing methods to enable potentially flexible deployment in miniaturized hardware configurations. Furthermore, our protocol manifests a high level of versatility, enabling multiple functions such as imaging as well as moving target tracking and identification. Moreover, the protocol utility extends to topographic laser profiling for comprehensive evaluation of 3D landscapes, further highlighting its remarkable adaptability. The versatility and adaptability of our protocol carry promise for even further extensions to such sophisticated, cutting edge applications as self-driving vehicles. Currently, our protocol is limited by its inability to obtain highly accurate angle measurements, providing only an approximate azimuth. We conjecture that optimizing signal sampling enables us to overcome this obstacle in the future, thereby further enhancing the protocol capacity and, by implication, its attractiveness for multiple applications.

AUTHOR DECLARATIONS

Conflict of Interest

The authors have no conflicts to disclose.

Author Contributions

Xiaofei Li: Conceptualization (equal); Methodology (equal); Writing – original draft (equal). **Sajjad Bashiri:** Formal analysis (equal); Writing – review & editing (equal). **Vasilisa Ponomarenko:** Formal analysis (equal); Writing – review & editing (equal). **Yu Wang:** Formal analysis (equal); Writing – review & editing (equal). **Yangjian Cai:** Funding acquisition (equal); Supervision (equal). **Sergey A. Ponomarenko:** Conceptualization (equal); Funding acquisition (equal); Supervision (equal); Writing – review & editing (equal).

DATA AVAILABILITY

The data that support the findings of this study are available from the corresponding authors upon reasonable request.

REFERENCES

[1]S. Tatsumi, K. Yamaguchi, and N. Furuya, "ForestScanner: A mobile application for measuring and mapping trees with LiDAR-equipped iPhone and iPad," Methods Ecol. Evol. **14**(7), 1603–1609 (2023).

[2]W. Shen, Y. Wang, Y. Lin, Y. Li, W. Jiang, and W. Hong, "Range-doppler based moving target image trace analysis method in circular SAR," Remote Sens. **15**(8), 2073 (2023).

[3]M. E. Weber, J. Y. N. Cho, and H. G. Thomas, "Command and control for multifunction phased array radar," IEEE Trans. Geosci. Remote Sens. **55**(10), 5899–5912 (2017).

[4]U. Germann, M. Boscacci, L. Clementi, M. Gabella, A. Hering, M. Sartori, I. V. Sideris, and B. Calpini, "Weather radar in complex orography," Remote Sens. **14**(3), 503 (2022).

[5]X. Zhang, K. Kwon, J. Henriksson, J. Luo, and M. C. Wu, "A large-scale micro-electromechanical-systems-based silicon photonics lidar," Nature **603**(7900), 253–258 (2022).

[6]A. A. Borsah, M. Nazeer, and M. S. Wong, "Lidar-based forest biomass remote sensing: A review of metrics, methods, and assessment criteria for the selection of allometric equations," Forests **14**(10), 2095 (2023).

[7]I. Arasaratnam, S. Haykin, T. Kirubarajan, and F. A. Dilkes, "Tracking the mode of operation of multi-function radars," in *IEEE Conference on Radar* (IEEE, 2006).

[8] A. Charlish, F. Hoffmann, C. Degen, and I. Schlangen, "The development from adaptive to cognitive radar resource management," IEEE Aerosp. Electron. Syst. Mag. **35**(6), 8–19 (2020).

[9] J. E. Stailey and K. D. Hondl, "Multifunction phased array radar for aircraft and weather surveillance," Proc. IEEE **104**(3), 649–659 (2016).

[10] P. John-Baptiste, A. Brandewie, J. Vinci, K. Bell, J. T. Johnson, C. F. Neese, and M. Rangaswamy, "Multi-task tracking and classification with an adaptive radar," IET Radar, Sonar Navig. **16**(4), 692–703 (2022).

[11] P. Zhang, J. Yan, W. Pu, H. Liu, and M. S. Greco, "Multi-dimensional resource management scheme for multiple target tracking under dynamic electromagnetic environment," IEEE Trans. Signal Process. **72**, 2377 (2024).

[12] J. Lin, J. Hu, Z. Xie, Y. Zhang, G. Huang, and Z. Chen, "A multitask network for people counting, motion recognition, and localization using through-wall radar," Sensors **23**(19), 8147 (2023).

[13] J. Zhao, H. Xu, H. Liu, J. Wu, Y. Zheng, and D. Wu, "Detection and tracking of pedestrians and vehicles using roadside lidar sensors," Transp. Res. Part C **100**, 68–87 (2019).

[14] B. Tang and P. Stoica, "MIMO multifunction RF systems: Detection performance and waveform design," IEEE Trans. Signal Process. **70**, 4381–4394 (2022).

[15] Z. Zhang, Y. Yuan, W. Yi, and J. Yan, "Quality of service-based multi-task scheduling for cooperative multi-radar systems," in *12th International Conference on Control, Automation and Information Sciences (ICCAIS)* (IEEE, 2023), pp. 477–482.

[16] L. Allen, M. W. Beijersbergen, R. J. C. Spreeuw, and J. P. Woerdman, "Orbital angular momentum of light and the transformation of Laguerre-Gaussian laser modes," Phys. Rev. A **45**(11), 8185 (1992).

[17] K. Liu, Y. Cheng, Z. Yang, H. Wang, Y. Qin, and X. Li, "Orbital-angular-momentum-based electromagnetic vortex imaging," Antennas Wireless Propag. Lett. **14**, 711–714 (2015).

[18] J. Wang, K. Liu, Y. Cheng, and H. Wang, "Vortex SAR imaging method based on OAM beams design," IEEE Sens. J. **19**(24), 11873–11879 (2019).

[19] R. Mao, K. Liu, H. Liu, Y. Yang, and H. Xiao, "Electromagnetic vortex imaging based on oam multiplexing beam with orthogonal polyphase coding," IEEE Sens. J. **23**, 30786 (2023).

[20] C. Li, S. Li, D. You, W. Peng, J. Li, Y. Li, Q. Li, and Z. Chen, "Targets'radial and tangential velocities estimation based on vortex electromagnetic waves," Remote Sens. **14**(16), 3861 (2022).

[21] J. Liang, Q. Zhang, Y. Luo, H. Yuan, and Y. Chen, "Three-dimensional imaging with bistatic vortex electromagnetic wave radar," Remote Sens. **14**(13), 2972 (2022).

[22] T. Jiang, J. Hu, S. Luo, Y. Wang, and W. Wu, "A fast and super-resolution method of vortex-based imaging," IEEE Antennas Wireless Propag. Lett. **22**, 2225–2229 (2023).

[23] J. W. Goodman, *Introduction to Fourier Optics* (Roberts and Company Publishers, 2005).

[24] P. Dong and Q. Chen, *LiDAR Remote Sensing and Applications* (CRC Press, 2017).

[25] Z. Gharineiat, F. T. Kurdi, and G. Campbell, "Review of automatic processing of topography and surface feature identification LiDAR data using machine learning techniques," Remote Sens. **14**(19), 4685 (2022).